RESEARCH ARTICLE

NANO · MICRO small
www.small-journal.com

Precise Control of Metal Active Sites of Metal–Organic Framework Nanozymes for Achieving Excellent Enzyme-Like Activity and Efficient Pancreatitis Therapy

Jie Zhang, Meilin Guo, Qikuan He, Zhisen Zhang, Boda Wu, Hongji Wu, Rizhao Li, Qiyu Zhang, Yonghua Tang, Youhui Lin,* and Yuepeng Jin**

Acute pancreatitis (AP) is a potentially life-threatening inflammatory disease that can lead to the development of systemic inflammatory response syndrome and its progression to severe acute pancreatitis. Hence, there is an urgent need for the rational design of highly efficient antioxidants to treat AP. Herein, an optimized Cu-based metal–organic framework (MOF) nanozyme with exceptional antioxidant activity is introduced, designed to effectively alleviate AP, by engineering the metal coordination centers in MN2Cl2 (M = Co, Ni, Cu). Specifically, the Cu MOF, which benefits from a Cu active center similar to that of natural superoxide dismutase (SOD), exhibited at least four times higher SOD-like activity than the Ni/Co MOF. Theoretical analyses further demonstrate that the CuN2Cl2 site not only has a moderate adsorption effect on the substrate molecule •OOH but also reduces the dissociation energy of the product H_2O_2. Additionally, the Cu MOF nanozyme possesses the excellent catalase-like activity and •OH removal ability. Consequently, the Cu MOF with broad-spectrum antioxidant activity can efficiently scavenge reactive oxygen species to alleviate arginine-induced AP. More importantly, it can also mitigate apoptosis and necrosis of acinar cells by activating the PINK1/PARK2-mediated mitophagy pathway. This study highlights the distinctive functions of tunable MOF nanozymes and their potential bio-applications.

1. Introduction

As an inflammatory problem of the pancreas, acute pancreatitis (AP) has evolved into the primary cause of hospitalization for gastrointestinal disorders worldwide.[1] Around 20% of patients with AP progress to severe acute pancreatitis (SAP) within a short period. This progression is characterized by pancreatic necrosis, remote organ dysfunction, and systemic inflammatory response syndrome, resulting in a mortality rate of up to 40%.[2,3] Anecdotal evidence suggests that oxidative stress plays an inevitable role in the progression of AP.[4] This is attributed to a disruption in the balance between intrinsic oxidative and antioxidative systems, leading to the overproduction of free radicals from associated reactive oxygen species (ROS).[5,6] In particular, the content of ROS shows a positive correlation with oxidative stress and can serve as a reflection of the severity of AP.[7,8] Therefore, maintaining the equilibrium between the production and elimination of ROS is crucial for minimizing oxidative damage to DNA, proteins, and lipids, thereby slowing down the progression from AP to SAP.[9]

Mitochondria, the central "power station" for cellular metabolism, are impaired in the early stages of AP. Moreover, mitochondria are potent organelles that eliminate ROS and damage-associated molecular patterns, thereby alleviating inflammation.[10] This feature makes them an ideal target for interventions in AP. Importantly, impaired

J. Zhang, M. Guo, Q. He, H. Wu, R. Li, Q. Zhang, Y. Jin
Department of Hepatobiliary and Pancreatic Surgery
The First Affiliated Hospital of Wenzhou Medical University
Wenzhou, Zhejiang 325000, P. R. China
E-mail: jinyuepeng@wzhospital.cn

Z. Zhang, Y. Tang, Y. Lin
Department of Physics
Research Institute for Biomimetics and Soft Matter
Fujian Provincial Key Laboratory for Soft Functional Materials Research
Xiamen University
Xiamen 361005, P. R. China
E-mail: 19820190154698@stu.xmu.edu.cn; linyouhui@xmu.edu.cn

M. Guo, Q. He, H. Wu, R. Li
Wenzhou Medical University
Wenzhou, Zhejiang 325000, P. R. China

B. Wu
Department of Ultrasonography
The First Affiliated Hospital of Wenzhou Medical University
Wenzhou, Zhejiang 325000, P. R. China

The ORCID identification number(s) for the author(s) of this article can be found under https://doi.org/10.1002/smll.202310675

DOI: 10.1002/smll.202310675

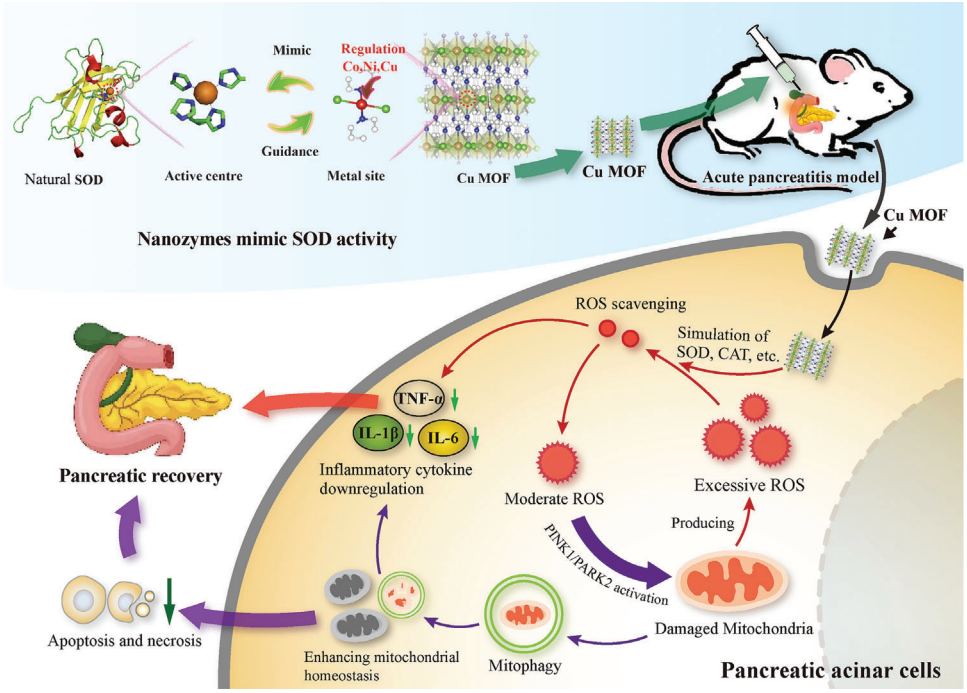

Scheme 1. Schematic diagram of Cu MOF nanozyme synthesis and its application in treating acute pancreatitis.

mitochondria can further exacerbate oxidation, underscoring the significance of functional mitochondria in ROS clearance. Recently, it was demonstrated that mitophagy regulates mitochondrial quantity and quality primarily through the PINK1/PARK2-dependent pathway.[11] Moreover, ROS accumulation is a primary factor in triggering mitophagy.[12] Accordingly, comparable changes occur throughout the duration of AP, and innovative approaches to activate mitophagy will undoubtedly help alleviate the severity of AP. Despite the evolution of medical policies in recent decades, their efficacy remains unsatisfactory. Therefore, it is imperative to develop effective strategies based on the internal mechanisms of AP to prevent progression and improve prognosis.

Current drugs targeting oxidative stress for the treatment of AP include bilirubin, octreotide, and plant extracts, such as curcumin, cyclophosphamide, and lycopene.[13–16] Although promising, their limited antioxidant capacity, as well as the complexity of their preparation and therapeutic processes, hinder their scavenging capabilities. Consequently, their clinical application remains challenging. On the other hand, catalytic antioxidants, such as artificial enzymes, have been demonstrated as alternatives to these traditional antioxidants. Artificial enzymes mimic the activities of various antioxidant enzymes and scavenge intracellular ROS, thereby alleviating inflammation.[17–19] Various nanomaterials have been explored for potential use as artificial nanoparticulate enzymes.[18,20–23] These materials offer specific advantages, such as tunable catalytic activity, high stability, and biocompatibility, making them suitable for biodetection and therapy.[18,23,24] Among these, metal–organic framework (MOF) nanomaterials, a relatively new type of porous solid material, have attracted significant research interest in catalysis owing to their well-defined coordination networks, mesoporous structures, and tunable porosities.[25,26] In particular, the diversity of metal nodes, connecting pillars, and the wide range of coordination interactions in all possible orientations make MOFs optimal substitutes for natural enzymes.[27,28] Thus, MOFs are expected to have great potential for the antioxidant treatment of inflammation.[29–31]

In this study, by engineering the metal coordination centers in MN2Cl2 (M = Co, Ni, or Cu), we present a facile strategy for fabricating an optimized Cu-based MOF (Cu-MOF) nanozyme that exhibits highly efficient ROS scavenging and alleviates oxidative stress (**Scheme 1**). Specifically, the superoxide dismutase (SOD)-like activity of the Cu MOF was at least four times higher than that of the Ni and Co MOFs. Theoretical analyses revealed that the CuN2Cl2 active site within the Cu MOF exhibited a moderate adsorption effect on •OOH molecules. Meanwhile, the CuN2Cl2 active site attenuated the binding to the product H_2O_2, thus lowering the energy barrier for its dissociation. Furthermore, the Cu MOF nanozyme exhibited excellent catalase (CAT)-like activity and demonstrated effective removal of •OH compared to the Co and Ni MOF nanozymes. As expected, the Cu MOF nanozyme showed significant antioxidant and anti-inflammatory activities in the SAP animal model. Even more impressively, the Cu MOF not only scavenged ROS directly by its intrinsic enzyme-like activity in AP, but it also activated PINK1/PARK2-mediated mitophagy to maintain mitochondrial homeostasis and alleviate inflammation. In addition, the Cu MOF nanozyme terminated the apoptosis and necrosis of pancreatic acinar cells by removing excessively damaged mitochondria and scavenging newly generated ROS from local pancreatic sites. Overall, this study provides a new perspective for designing efficient antioxidant nanozymes and a promising strategy for the treatment of SAP.

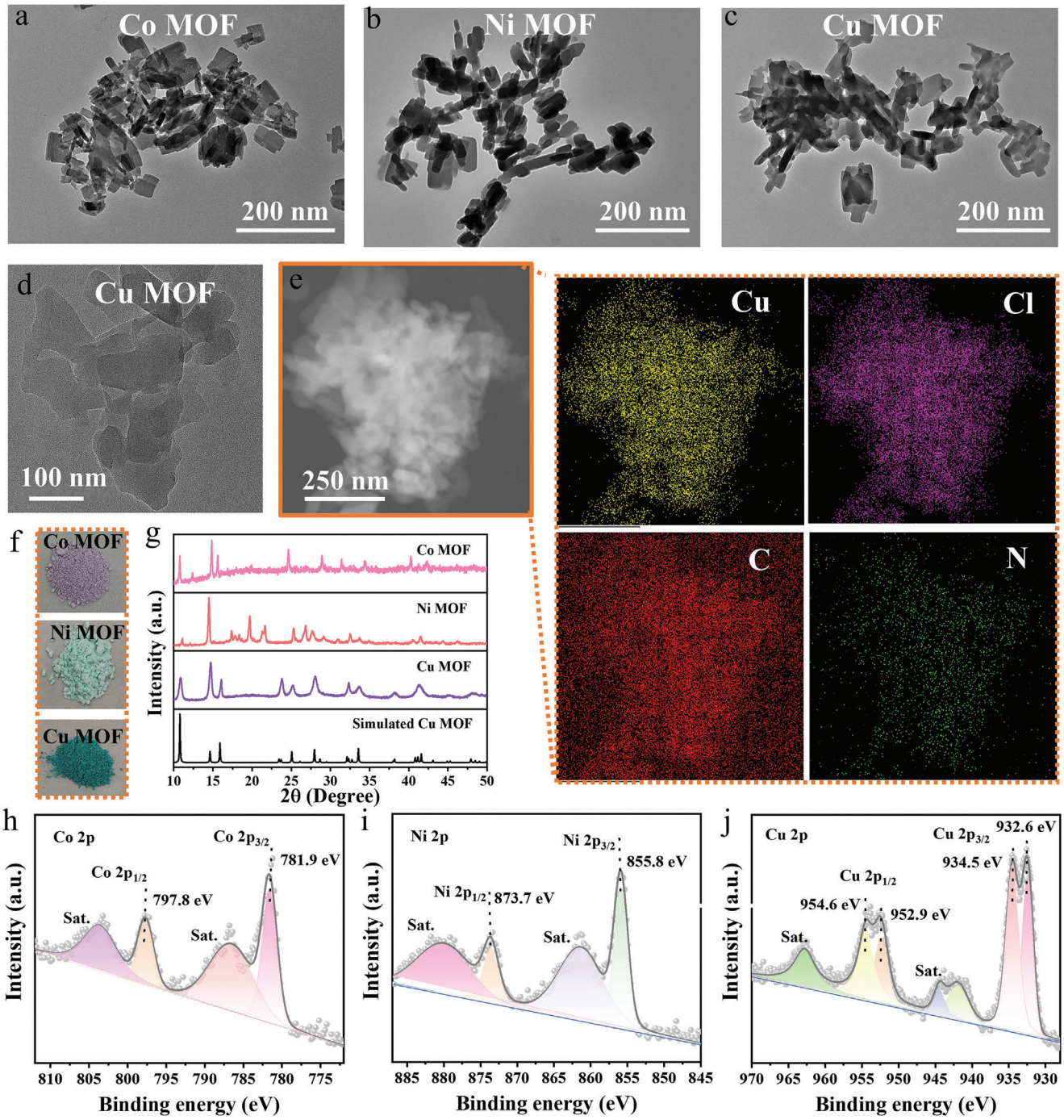

Figure 1. Structural characterization of M (Co, Ni, and Cu) MOF nanozymes. Transmission electron microscopy images: a) Co MOF; b) Ni MOF; c,d) Cu MOF. e) The corresponding energy-dispersive spectroscopy mapping images (Cu, yellow; Cl, purple; C, red; N, green). f) Photographs of M (Co, Ni, and Cu) MOF powder. g XRD patterns of M (Co, Ni, and Cu) MOF powder. XPS spectra: h) Co 2p; i) Ni 2p; j) Cu 2p.

2. Results and Discussion

2.1. Preparation and Characterization of the Cu MOF Nanozyme

Natural Cu-containing SOD has a Cu active center, which is essential for promoting the catalytic conversion of the substrate molecule •OOH to O_2 and H_2O_2. Therefore, we used Cu^{2+} and 4,4'-bipyridine (C10H8N2) as precursors in the synthetic system to construct a metal active center to mimic natural Cu-containing SOD.[32,33] As controls, Co MOF and Ni MOF with the same coordination environment were prepared using a similar synthesis strategy, with the only difference being the introduction of distinct metal precursors. The morphologies of Co and Ni MOFs are shown in **Figure** 1a,b as 2D nanosheets,

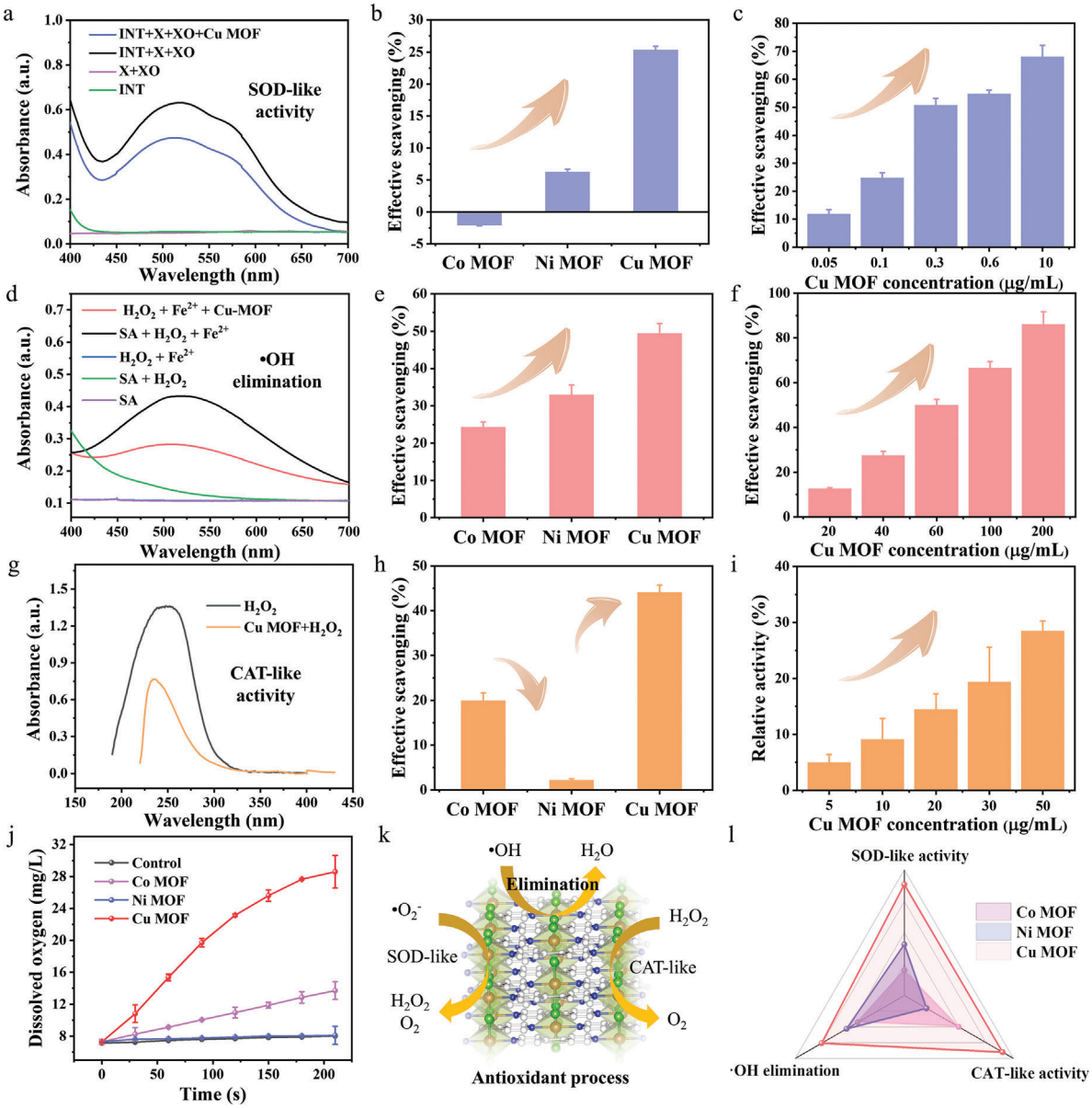

Figure 2. Antioxidative activity of M (Co, Ni, and Cu) MOFs. a) Absorption spectra of INT after reaction with X and XO in the absence and presence of Cu MOF. INT for iodonitrotetrazolium chloride, X for xanthine, and XO for xanthine oxidase. b) SOD-like activity. c) SOD-like activity at different concentrations of Cu MOF. d) Absorption spectra of salicylic acid after reaction with Fe^{2+}/H_2O_2 in the absence and presence of Cu MOF. e) •OH elimination activity. f) •OH elimination activity at different concentrations of Cu MOF. g) Absorption spectra of H_2O_2 at 235 nm during the catalytic elimination of H_2O_2 by Cu MOF. h) CAT-like activity. i) CAT-like activity at different concentrations of Cu MOF. j) Typical kinetic curves for the decomposition of H_2O_2 to produce oxygen in the presence of different concentrations of Cu MOF. k) Potential antioxidant reaction process of Cu MOF. l) Stellar plot of the antioxidant activity of M (Co, Ni, and Cu) MOFs. All error bars in the figures are averaged from three groups of parallel tests.

similar to those of Cu MOF (Figure 1c). Figure 1d shows that the size of the Cu MOF was ≈100 nm. In addition, elemental Cu, C, Cl, and N were evenly distributed in the Cu MOF, as observed from the energy-dispersive spectroscopy mapping (Figure 1e; Figure S1, Supporting Information). In contrast, the color of the sample powder varied according to the metal ions (Figure 1f). The X-ray diffraction (XRD) pattern of the experimentally synthesized Cu MOF agreed with that of the simulated Cu MOF structure (Figure 1g),[29,32] indicating that the theoretically chosen model was consistent with the crystal structure of the synthesized sample (Figure S2, Supporting Information). Notably, the XRD patterns of Co and Ni MOFs were somewhat different from the simulated XRD patterns, presumably due to other interactions between the metal ions and ligands.

X-ray photoelectron spectroscopy (XPS) was performed to identify the chemical composition of the M (Co, Ni, and Cu) MOFs and verify the existence of M (Co, Ni, and Cu), Cl, C, O, and N (Figure 1h–j; Figures S3–S5, Supporting Information). As shown in Figure 1j, the higher binding energy peak of the

Cu 2p spectrum at 934.5 eV was assigned to Cu^{2+}, accompanied by characteristic Cu^{2+} shakeup satellite peaks (962.6 and 941.8 eV).[34–36] The lower binding energy peak at 932.6 eV suggested the presence of Cu^{+} species. Collectively, the Cu MOF contained Cu in the states of Cu^{+} and Cu^{2+},[28] which is consistent with the valence state of Cu present in natural Cu-containing SOD. The chemical compositions of Co and Ni MOFs were further characterized using XPS. Figure 1h,i shows strong characteristic peaks for Co 2p in the Co MOF and Ni 2p in the Ni MOF, respectively. As expected, they all exhibited typical high-resolution characteristic spectra for elements such as C, N, O, and Cl, indicating that the added metal precursors had no effect on the formation of active metal sites during the self-assembly process (Figure 1h,i; Figures S4 and S5, Supporting Information). The atomic ratios of the surface elements of the samples further confirmed this result. As shown in Figure S6 (Supporting Information), the number of metal atoms on the surface of the M (Co, Ni, and Cu) MOF displayed a ratio of 1:2 with N and Cl, suggesting that the structure of the active sites in the crystals may be MN2Cl2. This is consistent with the crystal structure used for XRD analysis in our simulations. Therefore, we constructed the cell structures of Co and Ni MOFs in a similar way to the Cu MOF (Figures S7 and S8, Supporting Information).

2.2. SOD-Like, CAT-Like, and •OH Elimination Activity Assays

Since $\bullet O_2^-$ is one of the most destructive ROS, we first investigated the ability of the M (Co, Ni, Cu) MOF to remove $\bullet O_2^-$ (**Figure 2a–c**). First, $\bullet O_2^-$ was generated by xanthine and xanthine oxidase reactions. Then, the $\bullet O_2^-$ scavenging capacity of the M (Co, Ni, and Cu) MOF was characterized using the $\bullet O_2^-$-specific probe iodonitrotetrazolium chloride, which reacts with $\bullet O_2^-$ to produce a red product, whose solution exhibits a characteristic solid absorption at 505 nm (Figure 2a). In the presence of the Cu MOF, the intensity was significantly lower than that of the black line (Figure 2a, blue line), indicating that the Cu MOF effectively eliminated $\bullet O_2^-$. The SOD-like catalytic activity of the Cu MOF was time- and dose-dependent, with $\bullet O_2^-$ scavenging efficiency reaching almost 70% at a concentration of 10 μg mL^{-1} Cu MOF (Figure 2c; Figure S9, Supporting Information). Furthermore, the experimental order of SOD-like activity was Cu MOF > Ni MOF >> Co MOF (Figure 2b), which suggests that the central metal atoms are essential for nanozymes.

Generally, ROS produced at the site of inflammation include •OH and H_2O_2. To test whether the Cu MOF also eliminated •OH, we used absorption spectroscopy to detect •OH levels in the presence of the Cu MOF (Figure 2d–f). The Fenton reaction in the Fe^{2+}/H_2O_2 system generates •OH. The specific probe salicylic acid reacted with the hydroxyl group, and a clear absorption peak was observed at 520 nm (Figure 2d). Figure 2f and Figure S10 (Supporting Information) show that the elimination of •OH was enhanced as the concentration of the Cu MOF or the reaction time increased. We also compared the Cu MOF with the Co MOF or Ni MOF, demonstrating that the Cu MOF had the highest •OH scavenging activity (Figure 2e). In addition, both absorption spectroscopy and a dissolved oxygen meter were used to detect the CAT-like activity of the Cu MOF (Figure 2g–j). As shown in Figure 2g, pure H_2O_2 exhibited a characteristic solid absorption peak at ≈235 nm. In the presence of the Cu MOF, the absorption intensity was significantly reduced, suggesting that the Cu MOF exhibited H_2O_2 elimination activity (CAT-like activity). The CAT-like activity of the Cu MOF was concentration-dependent, and its relative activity could reach 30% using 50 μg mL^{-1} Cu MOF (Figure 2i). The H_2O_2 elimination ability of the Cu MOF was also higher than that of the Co and Ni MOFs (Figure 2h). This result was further confirmed by monitoring the oxygen content of the solutions (Figure 2j; Figure S11, Supporting Information). Both absorption spectroscopy and a dissolved oxygen meter revealed that the Cu MOF eliminated H_2O_2 and had excellent CAT-like properties.

Moreover, to verify that the ability of the Cu MOF to remove ROS was not from ions in solution, the ROS scavenging ability of individual Cu ions and ligand molecules was evaluated. The results are shown in Figure S12 (Supporting Information), and the ability of individual Cu ions and ligand molecules to scavenge ROS was negligible. Moreover, we found that the oxidase- and peroxidase-like activities were insignificant compared to the antioxidant activity of the Cu MOF (Figures S13 and S14, Supporting Information), suggesting that the Cu MOF does not produce sufficient amounts of ROS to damage normal cells, even after uptake by normal tissues during in vivo treatment. The mechanism underlying the antioxidant activity of the Cu MOF is shown schematically in Figure 2k. All the results showed that the Cu MOF has optimal enzyme-like activity (Figure 2l) along with the greatest therapeutic effects in ROS-induced inflammatory disease among the M (Co, Ni, Cu) MOFs.

To explore the origin of the excellent activity of the Cu MOF, we first performed N_2 adsorption-desorption experiments. For N_2 adsorption measurements, Brunauer–Emmett–Taylor analyses and the associated pore size distributions (Figure S15 and Table S1, Supporting Information) showed that the M (Co, Ni, Cu) MOFs had a porous structure, which was beneficial for the exposure of metal active sites. The Cu MOF has a smaller specific surface area and pore size than the Co MOF. However, the enzyme-like activity of the Cu MOF was higher than that of the Co MOF (Figure 2l), indicating that the activity difference in the M (Co, Ni, Cu) MOFs was not solely attributed to the specific surface area and pore size. Instead, it is more likely associated with disparities in the active sites themselves.

2.3. Density Functional Theory (DFT) Study of the SOD-Like Activity of M (Co, Ni, and Cu) MOFs

To further elucidate the reason for the enhanced Cu MOF SOD-like activity, we performed DFT calculations for the disproportionation of $\bullet O_2^-$ (a characteristic substrate of SOD) at the metal sites under alkaline conditions. In particular, the $\bullet O_2^-$ is a Brønsted base with $pK_b = 9.12$.[37] Therefore, it readily traps a proton from water to form •OOH and OH^- as shown in the following equation:

$$\cdot O_2^- + H_2O \rightarrow \cdot OOH + OH^- \quad (1)$$

Therefore, we used •OOH molecules as substrates for SOD-like activity in all our calculations. The top and side views of

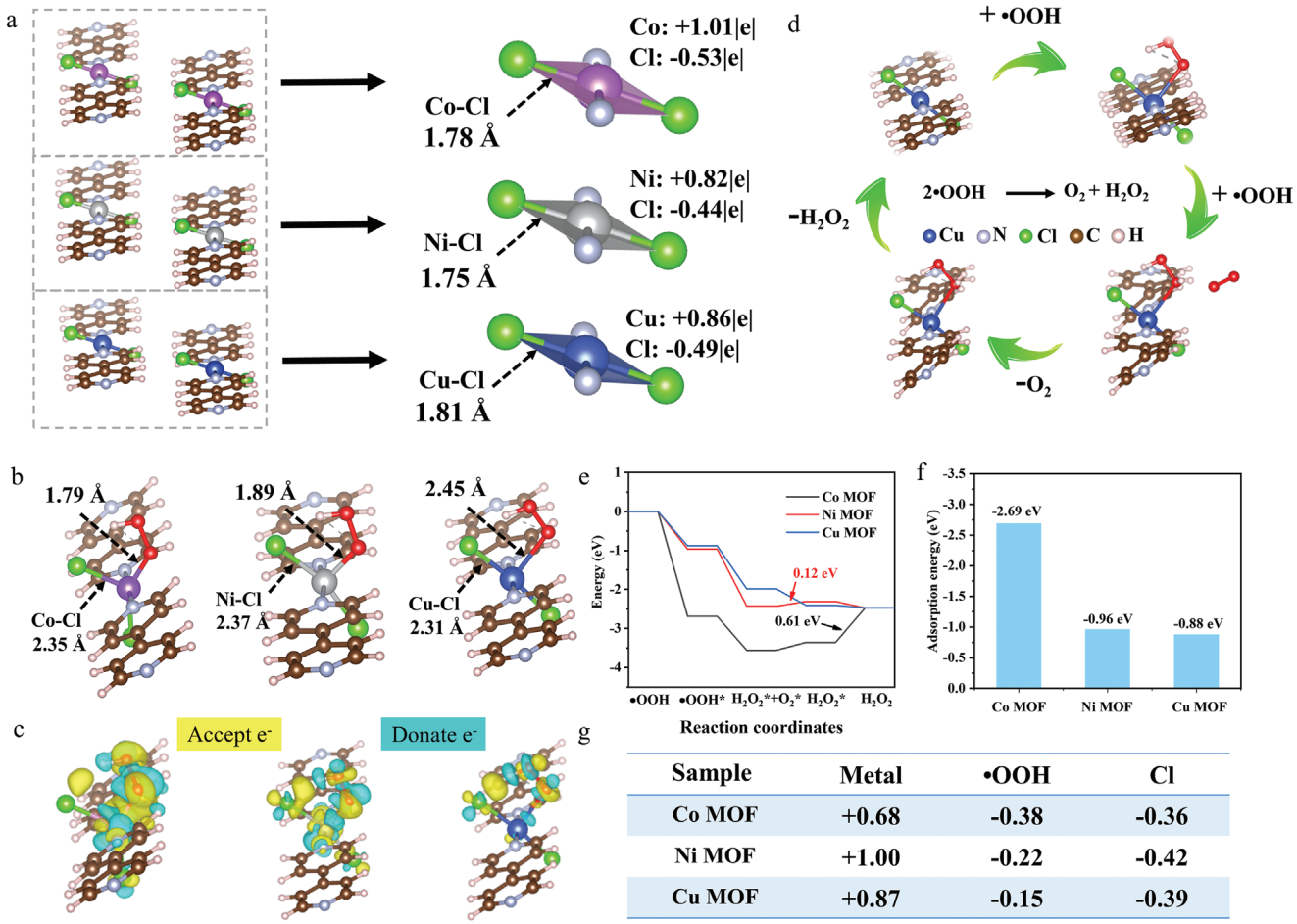

Sample	Metal	•OOH	Cl
Co MOF	+0.68	-0.38	-0.36
Ni MOF	+1.00	-0.22	-0.42
Cu MOF	+0.87	-0.15	-0.39

Figure 3. Theoretical studies on the mechanism of M (Co, Ni, and Cu) MOF SOD-like activity. a) The optimized cell structure of M (Co, Ni, and Cu) MOFs. b) •OOH* adsorption configuration on the M (Co, Ni, and Cu) MOF surface. c) Calculated charge density differences of M (Co, Ni, and Cu) MOF—OOH*. d) Proposed reaction process for Cu MOF. e) Energy diagram of the proposed reaction process for M (Co, Ni, and Cu) MOF models. f) Adsorption energies for •OOH adsorption on M (Co, Ni, and Cu) MOF surfaces. g) The Bader charge of •OOH adsorbed on the M (Co, Ni, and Cu) MOF models.

the cell structure of the Cu MOF showed that it was a 2D structure, such as graphene and molybdenum disulfide (Figures S2, S7, and S8, Supporting Information). Therefore, our computational model selected the 001 surfaces of M (Co, Ni, and Cu) MOFs to study the enzyme-like activity. In addition, based on our experimental data from XRD and the elemental content analysis of XPS, three surface models—Co, Ni, and Cu slabs—were constructed for the calculations (Figure S16, Supporting Information). As shown in **Figure** 3a, the M (Co, Ni, and Cu) MOFs had a similar coordination configuration. Still, the bond lengths of Co—Cl (1.78 Å) and Ni—Cl (1.75 Å) were shorter than that of Cu—Cl (1.81 Å). Simultaneously, the Cu site experienced a modest reduction in the number of electrons compared to the Co and Ni sites, which may be favorable for a moderate interaction of the Cu site with the substrate molecule. After adsorption of •OOH molecules, the M—Cl is extended to ≈2.3 Å (Figure 3b). Meanwhile, the order of the M–O bond lengths was Cu—O > Ni—O > Co—O, which indicates that the Co site has the strongest interaction with •OOH, followed by the Ni site, and the weakest is the Cu site, which is consistent with the results of the differential charge density maps (Figure 3c). This result was further confirmed by Bader charge analysis, where only the Co sites gained electrons after the adsorption of •OOH (a large number of electrons gathered between Co—O bonds) (Figure 3g).

Figure 3e shows the energy profiles of the most favorable pathways for surface O_2 and H_2O_2 production via •OOH dissociation. Among these nanozymes, the adsorption energy of •OOH on the Co MOF surface was the strongest at −2.69 eV, followed by the Ni MOF with an adsorption energy of −0.96 eV, while the Cu MOF had the weakest adsorption energy of −0.88 eV (Figure 3f). The adsorbed •OOH readily decomposes from •OOH in solution into surface H_2O_2 and O_2 species ($2OOH \rightarrow H_2O_2 + O_2$),[38] and the thermodynamic process was favorable on all three models (Figure 3e). In contrast, the subsequent O_2 dissociation process was thermodynamically favorable only on the Cu slab, whereas the energy barriers on the Co and Ni slabs were 0.20 and 0.12 eV, respectively. Therefore, the order of SOD-like activity of the Cu slab considered in terms of reaction energy barriers was Cu MOF > Ni MOF >> Co MOF, which is in agreement with the results of our experiments (Figure 2b). Based on the above

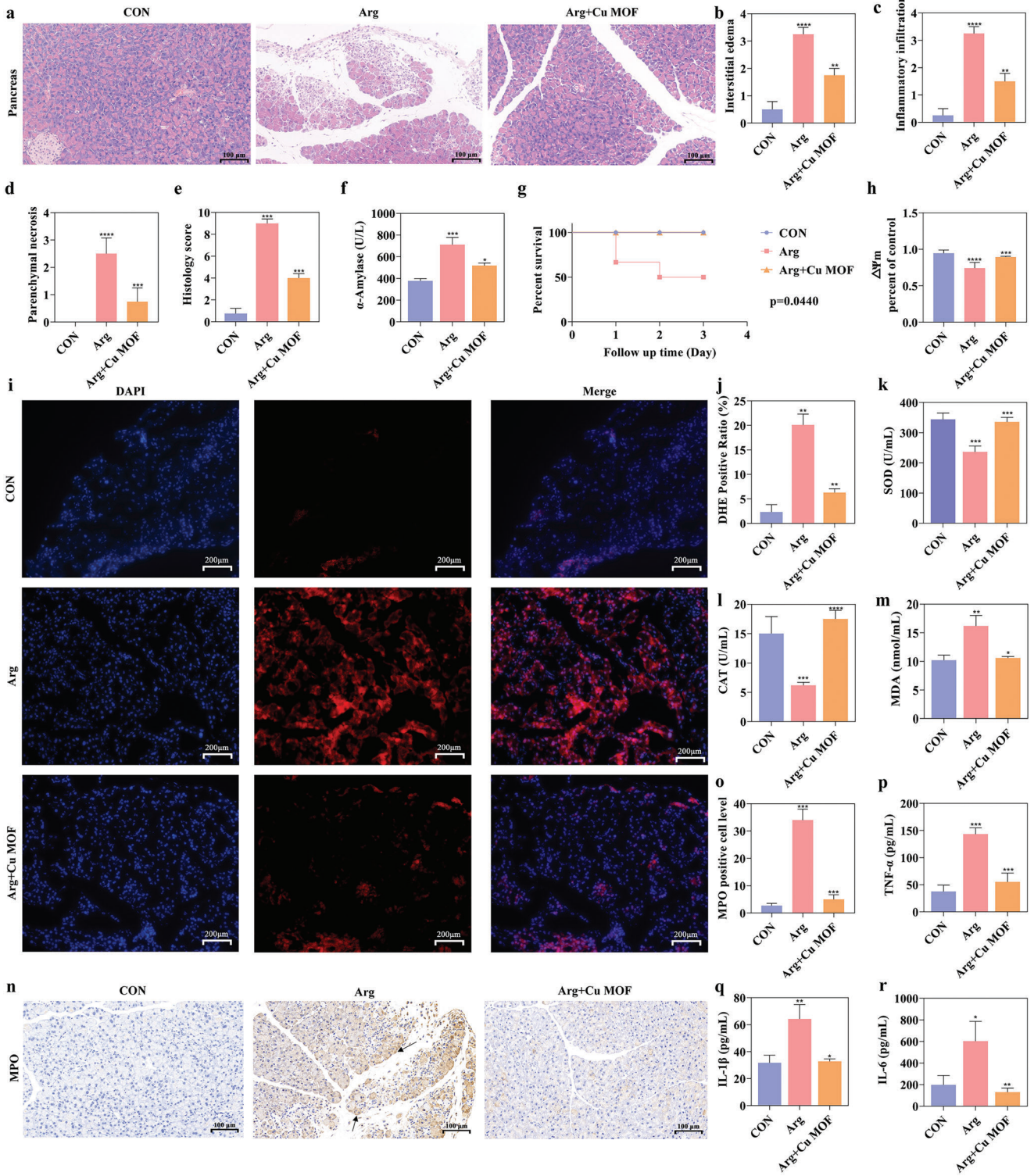

Figure 4. Cu MOF effectively alleviated pancreatic damage by modulating aggravated oxidative stress-induced inflammation in SAP. a) HE staining of pancreatic tissue. Scale bar: 50 μm. b) Interstitial edema histopathological score (n = 5). c) Inflammatory infiltration histopathological score (n = 5). d) Parenchymal necrosis histopathological score (n = 5). e) Histological analyses of pancreatic tissue (n = 5). f) Serum amylase analysis (n = 5). g) Survival curves of mice after different treatments (n = 5). h) Mitochondrial membrane potential of the pancreas (n = 5). i,j) The immunofluorescence analysis of the expression of ROS and quantitative analysis. Scale bar: 200 μm (n = 5). k–m) The levels of SOD, CAT, and malondialdehyde (MDA) changed in the various groups (n = 5). n–o) MPO expression was revealed by immunohistochemical staining of pancreatic tissues, and the quantitative data were shown (n = 5). Scale bar: 50 μm. p–r) Serum TNF-α, IL-1β, and IL-6 content (n = 5). The data are represented as mean values, and error bars indicate SEM (mean ± SEM). n represents the number of samples for each group ($^{*}p < 0.05$; $^{**}p < 0.01$; $^{***}p < 0.001$; $^{****}p < 0.0001$).

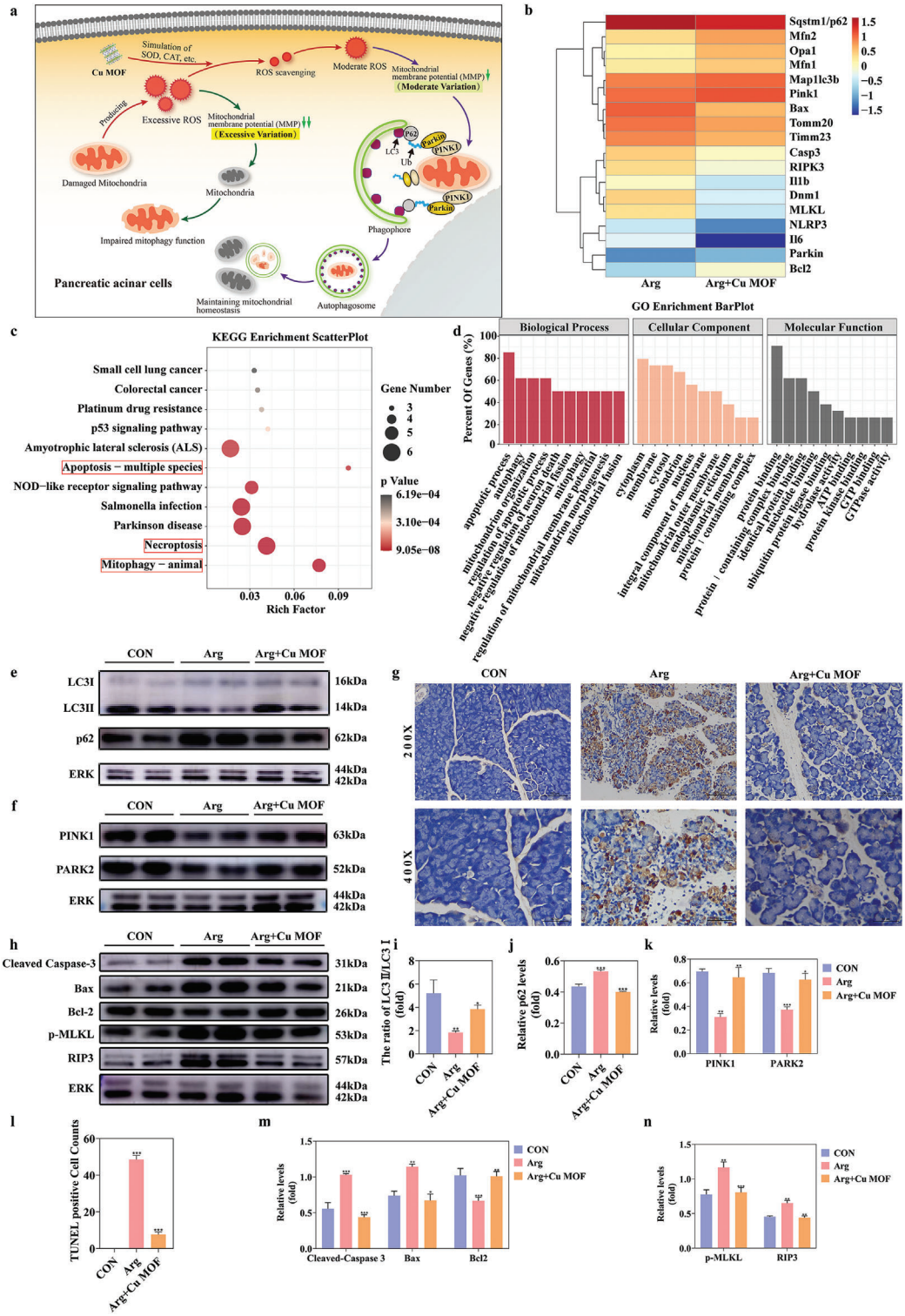

Figure 5. Cu MOF regulated PINK/PARK-mediated mitophagy to control ROS-induced inflammation and necroptosis. a) Schematic diagram of the mitophagy, anti-inflammatory, and antioxidant mechanisms of Cu MOF. b) Heatmap of the differentially expressed genes. c) Kyoto Encyclopedia of Genes and Genomes (KEGG) pathway terms. d) Significantly enriched Gene Ontology (GO) terms. e,i,j) Immunoblot analysis and quantification of p62 and LC3 in pancreatic tissues (n = 3). f,k) Immunoblot analysis and quantification of PINK1 and PARK2 in pancreatic tissues (n = 3). g,l) TUNEL positivity was revealed by immunohistochemical staining of pancreatic tissues and quantitative analysis (n = 3). Scale bar: 100 μm. h,m,n) Immunoblot analysis and quantification of cleaved caspase 3, Bax, Bcl-2, p-MLKL, and RIP3 in pancreatic tissues (n = 3). The data are represented as mean values, and error bars indicate SEM (mean ± SEM). n represents the number of samples for each group ($^{*}p < 0.05$; $^{**}p < 0.01$; $^{***}p < 0.001$; $^{****}p < 0.0001$).

calculations, a proposed reaction process for generating H_2O_2 and O_2 on the M (Co, Ni, and Cu) MOF surface is illustrated in Figure 3d.

2.4. The Cu MOF Effectively Alleviated Pancreatic Damage by Modulating Aggravated Oxidative Stress-Induced Inflammation in SAP

Oxidative stress, which occurs early in the development of AP, is closely linked to the necrosis of pancreatic acinar cells and exacerbates the systemic inflammatory response, ultimately resulting in SAP. Hence, the effective mitigation of oxidative stress may be a promising strategy to prevent AP progression to SAP and improve patient prognosis. Based on the broad-spectrum antioxidant activity of the as-prepared Cu MOF nanozymes, we evaluated their potential as antioxidants for treating SAP. An arginine (Arg)-induced SAP mouse model was established to explore the therapeutic potential of the Cu MOF, with a schematic diagram shown in Figure S17 (Supporting Information). Accordingly, histological analysis with hematoxylin-eosin(HE) staining indicated that the intraperitoneal Cu MOF injection could ameliorate pancreatic injury (**Figure 4**a), as well as interstitial edema (Figure 4b), inflammatory infiltration (Figure 4c), and parenchymal necrosis (Figure 4d), while improving the histological score (Figure 4e). Simultaneously, a decrease in serum α-amylase levels was observed following Cu MOF treatment in the Arg-SAP model (Figure 4f), indicating the potential anti-inflammatory effects of Cu MOF on pancreatic structures. In the case of SAP, the Cu MOF demonstrated a remarkable protective effect on both pancreatic tissue and distant organs. The microstructures of the lungs and kidneys, which are commonly affected organs in SAP, were examined using histological scores. These results consistently demonstrated a discernible trend following Cu MOF administration (Figures S18 and S19, Supporting Information), which further supports the potential therapeutic efficacy of the Cu MOF in mitigating the detrimental effects of SAP on distal organs. Furthermore, we conducted a more comprehensive evaluation to assess the impact of the Cu MOF on mortality in an Arg-induced SAP model. In particular, the Kaplan–Meier curve illustrated the effect of the Cu MOF on survival outcomes, with all mice remaining alive in the Arg + Cu MOF group compared to those in the SAP group at the time of sample collection (Figure 4g$p = 0.0440$).

Mitochondria play a vital role in maintaining cellular integrity and are closely associated with AP severity. In the early stages, exposure to inflammatory stimuli disrupts the mitochondrial membrane potential (MMP), leading to the release of mitochondrial contents and accelerating cell apoptosis and even necrosis.[39] As a determinant of ROS production,[40] MMP was evaluated using the JC-1 probe, and the statistical data demonstrated that the diminished MMP was restored by the Cu MOF in SAP (Figure 4h), implying that its protective effect was accomplished through mitochondrion-related mechanisms. Subsequently, we visualized and quantified the levels of ROS, which are byproducts of the mitochondrial respiratory chain, using immunofluorescence analysis (Figure 4i,j). The ROS level was significantly higher in the SAP model than in the control group and was remarkably reduced in the Cu MOF group, with a DHE-positive ratio. Because of the high SOD- and CAT-like activities of the optimal Cu MOF nanozyme in vitro, we further assessed the ability of the Cu MOF to scavenge excessive ROS in the Arg-SAP model. As shown in Figure 4, the levels of SOD and CAT in the SAP group exhibited a downward trend compared to those in the control group, indicating oxidative damage and an inflammatory response in the pancreas. However, the Cu MOF group demonstrated a higher serum concentration of both SOD and CAT than the SAP group (Figure 4k,l), verifying that the Cu MOF has unparalleled antioxidative and anti-inflammatory effects. Coincidently, the serum malondialdehyde (MDA) levels showed an opposite tendency, reflecting improved peroxidation-related damage in the SAP model treated with the Cu MOF (Figure 4m). As the inflammatory cascade can be further amplified via the interaction between ROS and pro-inflammatory cytokines, we evaluated the expression of pro-inflammatory factors. In contrast with the control group, the inflammation was more severe in SAP mice, as evidenced by a greater level of MPO and other serum inflammatory factors, such as TNF-α, IL-1β, and IL-6, which were suppressed by the Cu MOF (Figure 4n–r). Taken together, these results verified the superior antioxidant and anti-inflammatory capacities of the Cu MOF in SAP.

2.5. The Cu MOF Regulated PINK1/PARK2-Mediated Mitophagy to Control ROS-Induced Inflammation and Necroptosis in SAP

After confirming the significant antioxidant capacity of the Cu MOF in SAP, we conducted further exploration to determine whether there are other potential mechanisms to mitigate inflammation (**Figure 5**). RNA-seq was performed between the Arg and Arg + Cu MOF groups to unravel the underlying mechanism by which the Cu MOF orchestrates the dysregulated inflammatory cascade in SAP, with various differentially expressed genes identified in the heatmap (Figure 5b). Our analysis revealed a decrease in inflammatory cytokines IL-1β, IL-6, and NLRP3, as well as necrotic and apoptotic markers MLKL, cleaved caspase 3, and Bax in the Cu MOF group. Conversely, the expression of the anti-apoptotic protein Bcl2 increased, indicating the potential of the Cu MOF to inhibit inflammation, necrosis, and apoptosis in SAP. Additionally, autophagic mediators showed reduced expression of Sqstm1 (p62) and elevated expression of Map1lc3b compared to the SAP group, suggesting an enhanced level of autophagy following Cu MOF treatment. Intriguingly, in SAP with Cu MOF, the expression of mitochondrial membrane proteins TOMM20 and TIMM23 decreased, along with an increase in PINK1 and Parkin. These findings provide strong evidence for the clearance of dysfunctional mitochondria through selective autophagy, specifically through mitophagy. As previously documented, damaged mitochondria may cause mitophagy to degrade the generated debris and update biological functions.[41] Mitophagy maintains the mild stage of pancreatitis by preventing mitochondrial dysfunction, thereby ensuring that the disease remains self-limiting.[42] However, depending on the severity of the disease, impaired mitochondria-induced mitophagy has a dual function in AP.

Similarly, our previous studies confirmed that moderate ROS levels can activate mitophagy in acute pancreatitis. Excessive ROS may further inhibit mitophagy, provoking severe mitochondrial dysfunction and mitophagy impairment.[40] Combined with

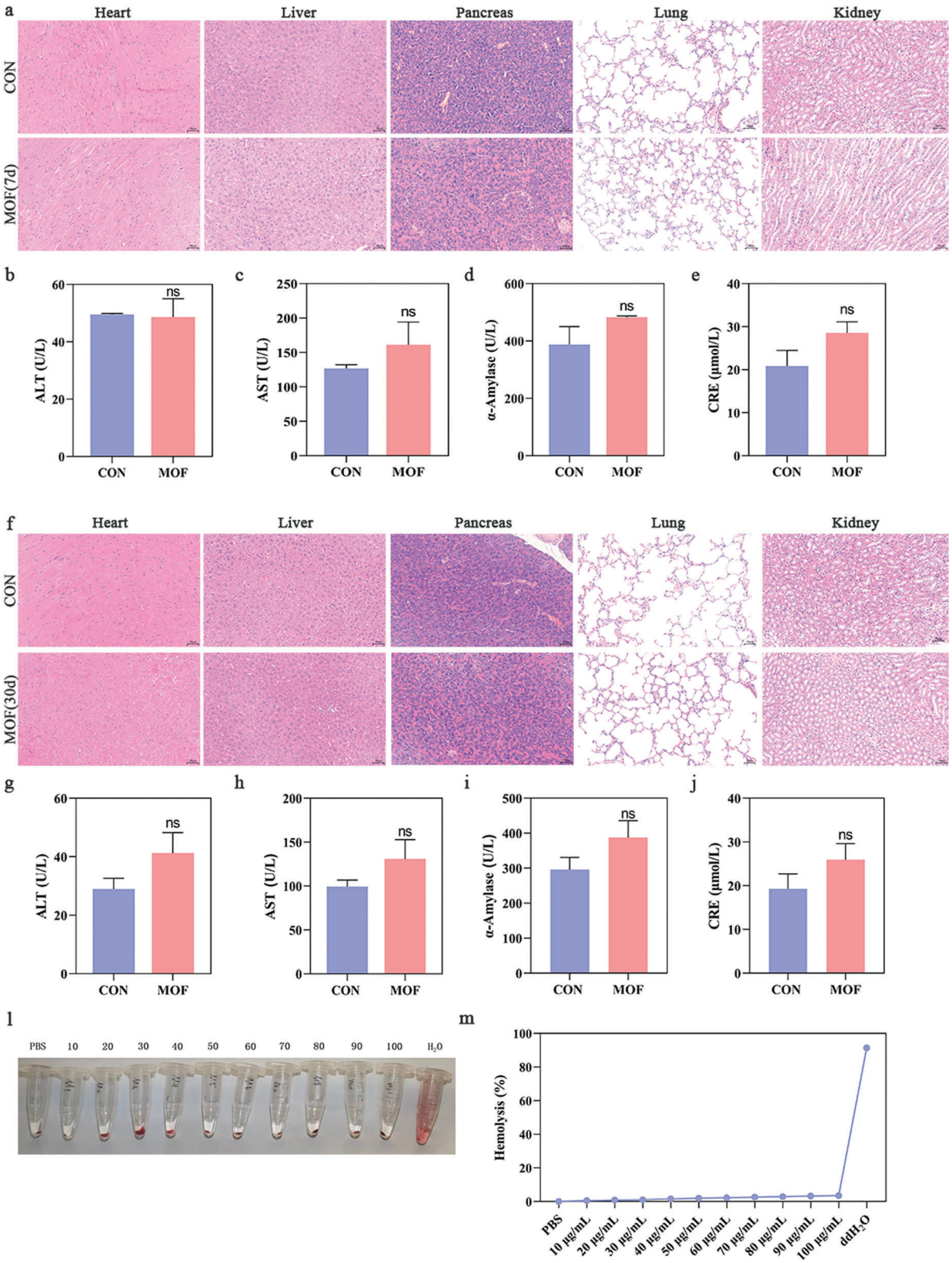

Figure 6. Biosafety of Cu MOF in vivo. a) HE staining of the heart, liver, pancreas, lung, and kidney tissues of mice after Cu MOF intraperitoneal administration at 7 days. Scale bars: 50 μm. b–e) The serum ALT, AST, amylase, and CREA levels changed at 7 days (n = 5). f) HE staining of the heart, liver, pancreas, lung, and kidney tissues of mice after Cu MOF intraperitoneal administration at 30 days. Scale bars: 50 μm. g–j) The serum ALT, AST, amylase, and CREA levels changed at 30 days (n = 5). k) Hemolysis test of Cu MOF. l) Hemolysis ratio of different concentrations of Cu MOF. The data are represented as mean values, and error bars indicate SEM (mean ± SEM). n represents the number of samples for each group.

Gene Ontology and Kyoto Encyclopedia of Genes and Genomes enrichment, the Cu MOF was suggested to be involved in the PINK1/PARK2-dependent mitophagy pathway, which may alleviate cellular apoptosis and necrosis (Figure 5c,d). Notably, despite numerous studies on mitophagy in AP, this is the first study to suggest that mitophagy can further alleviate the inflammatory cascade by treating cells with antioxidant nanozymes. Additionally, at the translational level, the expression of PINK1 and PARK2 exhibited a similar tendency after Cu MOF treatment, and the restored PARK2 was able to deliver ubiquitin to the mitochondria to develop autophagosomes by combining p62 and LC3B, resulting in mitophagy and clearance of damaged mitochondria with the autophagosome machinery.[43] Consistently, the effect of the Cu MOF on mitophagy, which suppressed SAP-induced necroptosis and inflammation, was validated by immunoblotting, as shown by the restored expression of LC3 II, Pink1, and Park2 and decreased p62 levels in the Arg + Cu MOF group compared to the Arg group (Figure 5e,f,i–k). In the animal model of AP, the total amount of ERK protein was constant; therefore, we used it as a loading control. Bizco et al. used ERK as a loading control in a study of mitochondrial function in pancreatitis.[44] The combination of ROS and pro-inflammatory substances may synergistically amplify the inflammatory cascade, leading to necrosis and apoptosis of acinar cells in SAP. Notably, the administration of the Cu MOF significantly suppressed necrosis, as evidenced by the reduced number of TUNEL-positive acinar cells (Figure 5g,l). Consistently, the protein expression levels of pro-apoptotic factors, including cleaved caspase 3 and Bax, as well as the anti-apoptotic index Bcl2, and necroptosis indicators p-MLKL and RIP3, showed similar patterns at the translational level (Figure 5h,m,n). These results reveal the involvement of the Cu MOF in mitophagy-mediated inflammation and necroptosis in SAP.

2.6. Safety Analysis of the Cu MOF In Vivo

Before their successful application in clinical transformation, it is crucial to conduct a biosecurity assessment of Cu MOFs. Given the limited biocompatibility commonly associated with Cu, we initially assessed the effect of the Cu MOF on hTERT-HPNE using the CCK-8 assay. The results validated that within the concentration of 100 μg mL^{-1}, there were no significant differences among the groups, suggesting the favorable biocompatibility of the Cu MOF at the cellular level (Figure S20, Supporting Information). To verify the safety of the Cu MOF in vivo, the Cu MOF (20 mg kg^{-1}) and normal saline were injected intraperitoneally into mice separately. Subsequently, several representative organs (the heart, liver, pancreas, lungs, and kidneys) and blood samples were collected on days 7 and 30 for HE staining and hematological parameters. The groups showed no significant morphological changes (**Figure 6**a,f). Furthermore, ALT, AST, α-amylase, and CREA after Cu MOF injection were in the normal range at both time intervals (Figure 6b–e,g–j). Various concentrations of the Cu MOF were added to erythrocytes from healthy mice and incubated for 4 h. Hemolysis was exclusively observed in the H_2O group (Figure 6k,l), indicating good compatibility.

3. Conclusion

In conclusion, we successfully developed an optimized Cu-based MOF nanozyme with exceptional antioxidant activity, designed to effectively alleviate AP, by engineering the metal coordination centers in MN2Cl2 (M = Co, Ni, Cu). The as-prepared product exhibited higher SOD-like activity than the Co and Ni MOFs. Moreover, the DFT results indicated that in the Cu MOF model, the Cu site had moderate adsorption energy for •OOH, which is conducive to lowering the dissociation energy barrier of H_2O_2 and thus increasing the SOD-like activity. The Cu MOF also had excellent CAT-like and •OH removal activities, which were superior to those of the Co and Ni MOFs. Furthermore, we demonstrated that the Cu MOF exhibited optimal SOD- and CAT-like activities to scavenge free radicals and favorable biocompatibility was observed through in vivo and in vitro assays. The potential antioxidative and anti-inflammatory properties of the Cu MOFs were identified by modulating PINK1/PARK2-dependent mitophagy. By removing excessively damaged mitochondria and generating ROS from local pancreatic sites, the Cu MOF nanozyme terminated inflammation, apoptosis, and necrosis in a murine model of SAP. This study provides a promising strategy for the development of efficient MOF-based nanozymes for the treatment of AP.

Supporting Information

Supporting Information is available from the Wiley Online Library or from the author.

Acknowledgements

J.Z., M.G., and Q.H. contributed equally to this work. This work was supported by the Key Laboratory of Diagnosis and Treatment of Severe Hepato-Pancreatic Diseases of Zhejiang Province (Grant No. 2018E10008), the National Nature Science Foundation (Grant No. 12274356), the Wenzhou Scientific Research Foundation Project (No. Y2023160), and Fundamental Research Funds for the Central Universities (20720220022), and the 111 Project (B16029).

Conflict of Interest

The authors declare no conflict of interest.

Data Availability Statement

The data that support the findings of this study are available from the corresponding author upon reasonable request.

Keywords

acute pancreatitis, metal–organic framework, mitophagy, nanozyme, reactive oxygen species

Received: November 20, 2023
Revised: February 28, 2024
Published online: March 15, 2024

[1] M. A. Mederos, H. A. Reber, M. D. Girgis, *JAMA, J. Am. Med. Assoc.* **2021**, *325*, 382.
[2] N. J. Schepers, O. J. Bakker, M. G. Besselink, U. Ahmed Ali, T. L. Bollen, H. G. Gooszen, H. C. van Santvoort, M. J. Bruno, *Gut* **2019**, *68*, 1044.
[3] J.-H. Tan, R.-C. Cao, L. Zhou, Z.-T. Zhou, H.-J. Chen, J. Xu, X.-M. Chen, Y.-C. Jin, J.-Y. Lin, J.-L. Zeng, S.-J. Li, M. Luo, G.-D. Hu, X.-B. Yang, J. Jin, G.-W. Zhang, *Theranostics* **2020**, *10*, 8298.
[4] S. M. Staubli, D. Oertli, C. A. Nebiker, *Crit. Rev. Clin. Lab. Sci.* **2015**, *52*, 273.
[5] Y. A. Hajam, R. Rani, S. Y. Ganie, T. A. Sheikh, D. Javaid, S. S. Qadri, S. Pramodh, A. Alsulimani, M. F. Alkhanani, S. Harakeh, A. Hussain, S. Haque, M. S. Reshi, *Cells* **2022**, *11*, 552.
[6] S. D. Crockett, S. Wani, T. B. Gardner, Y. Falck-Ytter, A. N. Barkun, *Gastroenterology* **2018**, *154*, 1096.
[7] K. Tsai, S. S. Wang, T. S. Chen, C. W. Kong, F. Y. Chang, S. D. Lee, F. J. Lu, *Gut* **1998**, *42*, 850.
[8] F. M. Abu-Zidan, M. J. Bonham, J. A. Windsor, *Br. J. Surg.* **2000**, *87*, 1019.
[9] P. J. Lee, G. I. Papachristou, *Nat. Rev. Gastroenterol. Hepatol.* **2019**, *16*, 479.
[10] I. V. Odinokova, K. F. Sung, O. A. Mareninova, K. Hermann, Y. Evtodienko, A. Andreyev, I. Gukovsky, A. S. Gukovskaya, *Gut* **2009**, *58*, 431.
[11] C. Tang, H. Han, M. Yan, S. Zhu, J. Liu, Z. Liu, L. He, J. Tan, Y. Liu, H. Liu, L. Sun, S. Duan, Y. Peng, F. Liu, X.-M. Yin, Z. Zhang, Z. Dong, *Autophagy* **2018**, *14*, 880.
[12] S. M. Jin, R. J. Youle, *Autophagy* **2013**, *9*, 1750.
[13] M. V. Butnariu, C. V. Giuchici, *J. Nanobiotechnol.* **2011**, *9*, 3.
[14] J. B. Hu, S. J. Li, X. Q. Kang, J. Qi, J. H. Wu, X. J. Wang, X. L. Xu, X. Y. Ying, S. P. Jiang, J. You, Y. Z. Du, *Carbohydr. Polym.* **2018**, *193*, 268.
[15] J. Xiong, J. Ni, G. Hu, J. Shen, Y. Zhao, L. Yang, J. Shen, G. Yin, C. Chen, G. Yu, Y. Hu, M. Xing, R. Wan, X. Wang, *J. Ethnopharmacol.* **2013**, *145*, 573.
[16] Z. Chen, C. T. Vong, C. Gao, S. Chen, X. Wu, S. Wang, Y. Wang, *Mol. Pharmaceutics* **2020**, *17*, 2260.
[17] B. Wang, Y. Fang, X. Han, R. Jiang, L. Zhao, X. Yang, J. Jin, A. Han, J. Liu, *Angew. Chem., Int. Ed.* **2023**, *62*, 202307133.
[18] Y. Huang, J. Ren, X. Qu, *Chem. Rev.* **2019**, *119*, 4357.
[19] H. Chen, T. Ye, F. Hu, K. Chen, B. Li, M. Qiu, Z. Chen, Y. Sun, W. Ye, H. Wang, D. Ni, L. Guo, *Sci. Adv.* **2023**, *9*, 0988.
[20] X. Ding, Z. Zhao, Y. Zhang, M. Duan, C. Liu, Y. Xu, *Small* **2023**, *19*, 2207142.
[21] I. Nath, J. Chakraborty, F. Verpoort, *Chem. Soc. Rev.* **2016**, *45*, 4127.
[22] H. Sun, Y. Zhou, J. Ren, X. Qu, *Angew. Chem., Int. Ed.* **2018**, *57*, 9224.
[23] J. Wu, X. Wang, Q. Wang, Z. Lou, S. Li, Y. Zhu, L. Qin, H. Wei, *Chem. Soc. Rev.* **2019**, *48*, 1004.
[24] H. Wang, K. Wan, X. Shi, *Adv. Mater.* **2019**, *31*, 1805368.
[25] D. Wang, D. Jana, Y. Zhao, *Acc. Chem. Res.* **2020**, *53*, 1389.
[26] H. C. Zhou, J. R. Long, O. M. Yaghi, *Chem. Rev.* **2012**, *112*, 673.
[27] G. Lan, Y. Fan, W. Shi, E. You, S. S. Veroneau, W. Lin, *Nat. Catal.* **2022**, *5*, 1006.
[28] M. Li, J. Chen, W. Wu, Y. Fang, S. Dong, *J. Am. Chem. Soc.* **2020**, *142*, 15569.
[29] Y. Tang, Y. Han, J. Zhao, Y. Lv, C. Fan, L. Zheng, Z. Zhang, Z. Liu, C. Li, Y. Lin, *Nano-Micro Lett.* **2023**, *15*, 112.
[30] L. He, G. Huang, H. Liu, C. Sang, X. Liu, T. Chen, *Sci. Adv.* **2020**, *6*, 9751.
[31] Y. Liu, Y. Cheng, H. Zhang, M. Zhou, Y. Yu, S. Lin, B. Jiang, X. Zhao, L. Miao, C. W. Wei, Q. Liu, Y. W. Lin, Y. Du, C. J. Butch, H. Wei, *Sci. Adv.* **2020**, *6*, 2695.
[32] N. Masciocchi, P. Cairati, L. Carlucci, G. Mezza, G. Ciani, A. Sironi, *J. Chem. Soc. Dalton Trans.* **1996**, *1996*, 2739.
[33] Y. Sheng, I. A. Abreu, D. E. Cabelli, M. J. Maroney, A. F. Miller, M. Teixeira, J. S. Valentine, *Chem. Rev.* **2014**, *114*, 3854.
[34] F. Xu, Y. Tang, H. Wang, H. Deng, Y. Huang, C. Fan, J. Zhao, C. Lin, Y. Lin, *Small* **2022**, *18*, 2201205.
[35] A. Bakandritsos, R. G. Kadam, P. Kumar, G. Zoppellaro, M. Medved, J. Tucek, T. Montini, O. Tomanec, P. Andryskova, B. Drahos, R. S. Varma, M. Otyepka, M. B. Gawande, P. Fornasiero, R. Zboril, *Adv. Mater.* **2019**, *31*, 1900323.
[36] J. Zhou, D. Xu, G. Tian, Q. He, X. Zhang, J. Liao, L. Mei, L. Chen, L. Gao, L. Zhao, G. Yang, W. Yin, G. Nie, Y. Zhao, *J. Am. Chem. Soc.* **2023**, *145*, 4279.
[37] X. Shen, W. Liu, X. Gao, Z. Lu, X. Wu, X. Gao, *J. Am. Chem. Soc.* **2015**, *137*, 15882.
[38] Z. Wang, J. Wu, J. J. Zheng, X. Shen, L. Yan, H. Wei, X. Gao, Y. Zhao, *Nat. Commun.* **2021**, *12*, 6866.
[39] R. Mukherjee, O. A. Mareninova, I. V. Odinokova, W. Huang, J. Murphy, M. Chvanov, M. A. Javed, L. Wen, D. M. Booth, M. C. Cane, M. Awais, B. Gavillet, R. M. Pruss, S. Schaller, J. D. Molkentin, A. V. Tepikin, O. H. Petersen, S. J. Pandol, I. Gukovsky, D. N. Criddle, A. S. Gukovskaya, R. Sutton, *Gut* **2016**, *65*, 1333.
[40] J. Zhang, W. Huang, Q. He, T. Deng, B. Wu, F. Huang, J. Bi, Y. Jin, H. Sun, Q. Zhang, K. Shi, *Free Radical Biol. Med.* **2021**, *166*, 147.
[41] D. N. Criddle, *J Physiol* **2019**, *597*, 5741.
[42] M. I. Vaccaro, F. Mitchell, F. Rivera, C. D. Gonzalez, *Adv. Protein Chem. Struct. Biol.* **2022**, *132*, 175.
[43] Q. Lin, S. Li, N. Jiang, X. Shao, M. Zhang, H. Jin, Z. Zhang, J. Shen, Y. Zhou, W. Zhou, L. Gu, R. Lu, Z. Ni, *Redox. Biol.* **2019**, *26*, 101254.
[44] G. Biczo, E. T. Vegh, N. Shalbueva, O. A. Mareninova, J. Elperin, E. Lotshaw, S. Gretler, A. Lugea, S. R. Malla, D. Dawson, P. Ruchala, J. Whitelegge, S. W. French, L. Wen, S. Z. Husain, F. S. Gorelick, P. Hegyi, Z. Rakonczay, I. Gukovsky, A. S. Gukovskaya, *Gastroenterology* **2018**, *154*, 689.